

Satellite Infall and the Growth of Bulges of Spiral Galaxies

M.C. Eliche-Moral, M. Balcells, J.A.L. Aguerri, & A.C. González-García

Proceeding of the Joint European and National Astronomical Meeting, "The Many Scales in the Universe", held in Granada, Spain, September 13-17, 2004.

Instituto de Astrofísica de Canarias, C/ Vía Láctea, E-38200 La Laguna, Tenerife, Spain. Contact: mcem@iac.es, balcells@iac.es, jalfonso@iac.es, cglez@iac.es

Abstract

For bulges of spiral galaxies, the concentration, or Sersic index, increases with bulge luminosity and bulge-to-disk ratio B/D (Andredakis, Peletier, & Balcells, 1995). Does this trend trace the growth of bulges via satellite accretion? And, is satellite infall consistent with this trend? Aguerri, Balcells, & Peletier (2001) (ABP01, hereandafter) investigated this question with N-body simulations of the accretion of dense, spheroidal satellites. Here, we expand on that work by running N-body simulations of the accretion of satellites that have realistic densities. Satellites are modeled as disk-bulge structures with their own dark-matter halo. A realistic density scaling with the primary galaxy is ensured by using the Tully-Fisher relation. Our merger models show that most satellites disrupt before reaching the center. However, a bulge-disk decomposition of the surface density profile after the accretion shows an increase of both the B/D and the Sersic index n of the bulge. The increase in the mass and concentration of the inner Sersic component is due to inward piling up of disk material due to transient bars during the satellite orbital decay. This research is described in Eliche-Moral et al. (2005).

1 N-body models

Both the primary and satellite galaxies comprise an exponential disk, a King-model bulge and a dark halo built as an Evans model. N-body realizations are built following Kuijken & Dubinski (1995). The satellite luminous mass scales with the mass of the initial bulge as 1:2, 1:3 and 1:6. Relative sizes, or densities, are determined by applying the Tully-Fisher to the primary and secondary. We experimented with α_{TF} exponents of 3, 3.5 and 4.0, although the exponent did not affect the main results. In total, we had 10 experiments. Orbital parameters for the merger experiments, satellite mass ratios and half-mass radii are given in Table 2.

Models were run using a TREECODE from Hernquist & Katz (1989), using 185,000 particles in each experiment. Masses, radii and number of particles are given in Table 1. In order to get structural parameters of the remnants, we performed Sérsic+exponential fits to the face-on azimuthally-averaged radial surface brightness profiles using a code described in Graham (2001). The Sérsic law was used for fitting the bulge (Sérsic, 1968; Graham, 2001; Möllenhoff & Heidt, 2001; MacArthur, Courteau, & Holtzman, 2002):

$$I(r) = I_e \cdot \exp \{b_n \cdot [(r/r_e)^{1/n} - 1]\} \quad (1)$$

where r_e is the half-light radius, I_e is the surface brightness at r_e and n is the Sérsic index. The factor b_n is a function of the concentration parameter n . An approximation that gives good results in the range $n < 10$ is $b_n = 1.9992 \cdot n - 0.3271$ (see Capaccioli, 1987; Graham, 2001). Disk contribution can be fitted with the exponential law:

$$I(r) = I_0 \cdot \exp(-r/h_D) \quad (2)$$

where h_D is the disk scale length and I_0 is its central surface brightness.

The final face-on, azimuthally-averaged radial surface density profiles of the luminous matter for all the models are shown in Figures 1b-k. Figures 1a is the surface density profile of the luminous matter for the primary galaxy. Dotted and dashed lines are the simultaneous two component fits performed to the total luminous surface density (exponential plus Sérsic-law). Residuals in magnitudes of the fits appear down its corresponding surface brightness profile in Figure 1. As can be seen, they are less than 0.15 mags in all the cases, a quite reasonable result compared to typical observational errors. Final fitted parameters and bulge-to-disk mass ratios derived from the fits are tabulated in Table 3.

Table 1: Initial parameters of the primary galaxy and the satellites.

NP (1)	Primary Galaxy			Satellites			Primary Galaxy Characteristics					
	Disk1 (2)	Bulge1 (3)	Hal01 (4)	Disk2 (5)	Bulge2 (6)	Hal02 (7)	M_{Bulge} (8)	M_{Disk} (9)	M_{Dark} (10)	r_B (11)	h_D (12)	z_D (13)
185K	40K	10K	90K	10K	5K	30K	0.42	0.82	5.20	0.195	1.0	0.1

Column description: (1) Total particle No. (2) No. of primary disk particles. (3) No. of primary bulge particles. (4) No. of primary halo particles. (5) No. of satellite disk particles. (6) No. of satellite bulge particles. (7) No. of satellite halo particles. (8) Primary bulge mass. (9) Primary disk mass. (10) Primary halo mass. (11) Primary bulge half-mass radius. (12) Disk truncation radius. (13) Disk scale height.

2 Growth of bulges

Figure 2 show growth vectors in the plane n vs. $\log(B/D)$, where the B/D ratios are derived from the Sérsic+exponential fits. Plotting points indicate the characteristics of our run models, according to the legend in the Figure. Real bulges from the samples of de Jong (1996b) (re-analysed by G01) and APB95 are drawn too, together with

Table 2: Orbital and scaling parameters for the merger experiments.

Model (1)	Code (2)	$M_{Sat}(Lum)/M_G(\text{Bulge})$ (3)	M_{Sat}/M_G (4)	α_{TF} (5)	R_{Sat}/R_G (6)	V_R (7)	V_θ (8)	θ_1 (9)
(1)	M2TF4D	1/2	0.16	4.0	0.4	-0.00142	0.24873	30
(2)	M2TF35D	1/2	0.16	3.5	0.46	-0.00142	0.24873	30
(3)	M2TF3D	1/2	0.16	3.0	0.54	-0.00142	0.24873	30
(4)	M3TF4D	1/3	0.11	4.0	0.33	-0.00131	0.24331	30
(5)	M3TF35D	1/3	0.11	3.5	0.39	-0.00131	0.24331	30
(6)	M3TF3D	1/3	0.11	3.0	0.48	-0.00131	0.24331	30
(7)	M6D	1/6	0.05	3.5	0.28	-0.00029	0.23664	30
(8)	M2R	1/2	0.16	3.5	0.46	-0.00142	0.24873	150
(9)	M3R	1/3	0.11	3.5	0.39	-0.00131	0.24331	150
(10)	M6R	1/6	0.05	3.5	0.28	-0.00029	0.23664	150

Column description: (1) Model number. (2) Model code. (3) Initial mass ratio between luminous satellite material and primary bulge material. (4) Initial mass ratio between satellite and primary galaxy. (5) Tully-Fisher index for scaling. (6) Initial half-mass radius ratio between satellite and bulge. (7) and (8) Radial and tangential velocity components of the relative orbit. (9) Initial angle between the orbital momentum and the primary disk spin. The other three angles involved in the orbits are fixed: $\phi_1=0^\circ$, $\theta_2=25^\circ$, and $\phi_2=90^\circ$.

Table 3: Fitted parameters for Sérsic bulge plus exponential disk decomposition of the final remnants.

Model (1)	Code (2)	χ^2 (mag) (3)	Disk		Bulge			B/D (9)
			$\log(\mu_0)$ (4)	h_D (5)	$\log(\mu_e)$ (6)	r_e (7)	n (8)	
Initial	...	0.037	-0.87±0.01	1.05±0.02	0.01±0.04	0.199±0.02	0.92±0.21	0.50
(1)	M2TF3D	0.053	-0.99±0.05	1.19±0.03	0.14±0.02	0.187±0.03	1.80±0.16	0.83
(2)	M2TF35D	0.035	-0.95±0.02	1.13±0.02	0.23±0.06	0.169±0.01	2.01±0.23	0.89
(3)	M2TF4D	0.039	-0.99±0.02	1.16±0.05	0.18±0.01	0.179±0.03	2.09±0.15	0.94
(4)	M3TF3D	0.047	-0.92±0.03	1.11±0.04	0.13±0.02	0.185±0.03	1.32±0.09	0.66
(5)	M3TF35D	0.035	-0.97±0.01	1.15±0.06	0.21±0.03	0.172±0.02	1.69±0.11	0.80
(6)	M3TF4D	0.048	-0.98±0.02	1.17±0.05	0.11±0.01	0.193±0.05	1.45±0.11	0.75
(7)	M6D	0.089	-0.88±0.07	1.06±0.03	0.14±0.02	0.181±0.04	1.18±0.13	0.63
(8)	M2R	0.066	-0.80±0.04	0.97±0.02	0.13±0.04	0.184±0.03	1.63±0.17	0.72
(9)	M3R	0.062	-0.85±0.04	1.03±0.06	0.23±0.05	0.162±0.04	2.04±0.13	0.78
(10)	M6R	0.040	-0.90±0.01	1.09±0.07	0.22±0.02	0.163±0.04	1.58±0.12	0.68

Column description: (1) Model number. (2) Model code. (3) χ^2 of the fit. (4) Disk central intensity. (5) Disk scale length. (6) Bulge effective surface density. (7) Bulge effective radius. (8) Bulge profile Sérsic index. (9) Bulge-to-disk mass ratio derived from the Sérsic+exponential fit.

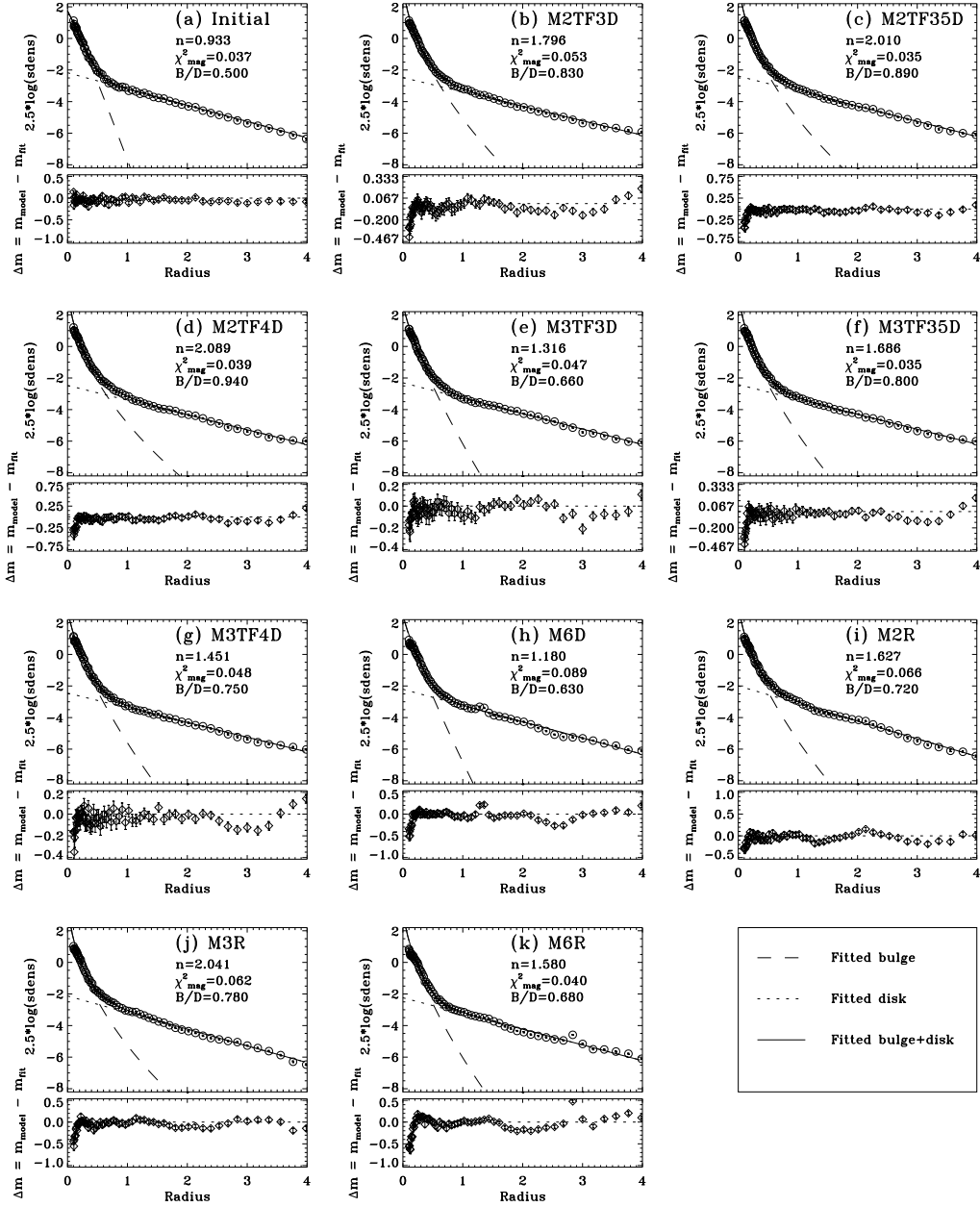


Figure 1: Radial surface density profiles of luminous matter and Sérsic+exponential simultaneous fits. *Upper panels of each frame*: Surface density distributions and performed fits. Panels: (a) Initial model. (b-h) Prograde models after the merger is complete. (i-k) Retrograde models after the merger is complete. *Open circles*: model measurements. *Dashed line*: Sérsic $r^{1/n}$ fitted component. *Dotted lines*: Exponential fitted component. *Solid lines*: Sum of the two fitted components. *Lower panels of each frame*: Residuals in magnitudes. Error bars of model measurements in magnitudes are plotted upon the residual points (*diamonds*).

the growth vectors of ABP01 high-density models (diamond points) for comparison. Growth vectors in the plane n vs. B/D show a similar dependence to the one found

by ABP01: $\mu(r)$ evolves quickly from an initial exponential bulge $n \sim 1$ to earlier types bulges in all the cases, reaching $n=2.1$, and proportionally to the satellite mass. Then, not only high-density, but also low-density satellite accretion onto disk-bulge-halo galaxies causes the bulge surface brightness profile to evolve toward higher- n Sersic profiles, following similar increasing trends and values for the Sersic index n with B/D ratios just as in the observations. The low-density experiments fill the region in the plane n vs. B/D that ABP01 high-density experiments left empty.

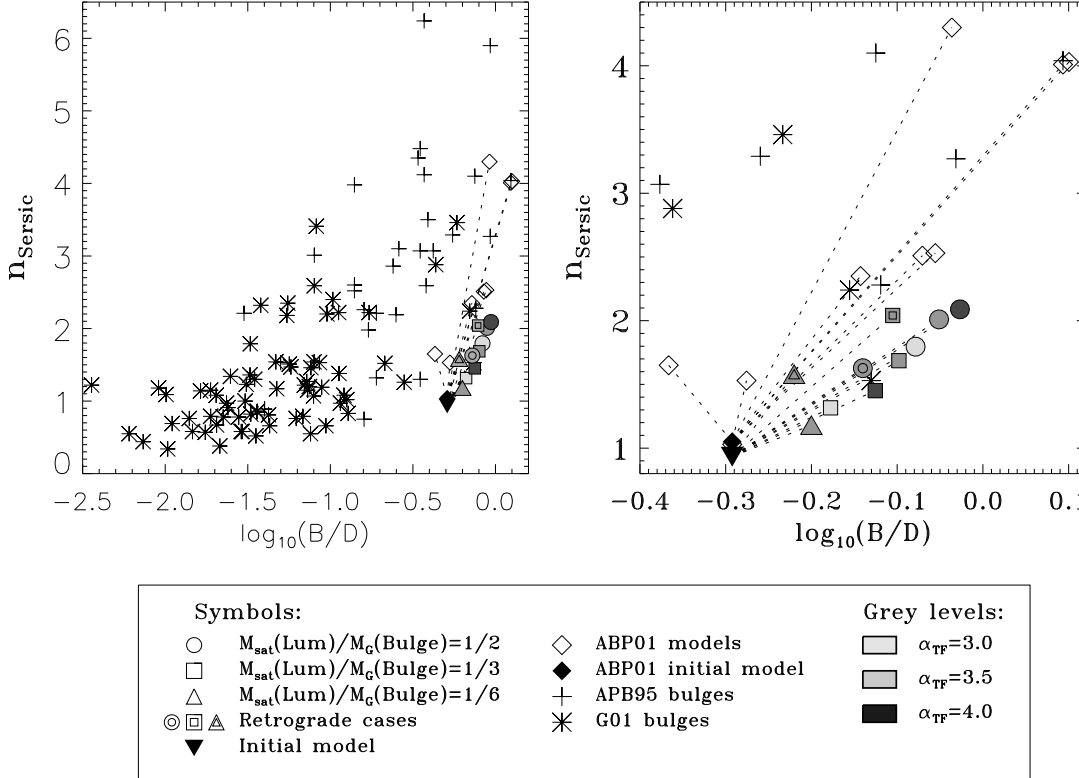


Figure 2: Growth vectors in the n - $\log(B/D)$ plane for the present low-density models. Right panel shows a zoom of the region from the left panel where our models are. Each arrow starts at the location of the original model and ends at the n and B/D derived from the two-component fit to the surface density profile after the merger. Growth vectors of ABP01 high-density models are plotted for comparison. Distributions of n vs. $\log(B/D)$ for bulges of several studies are drawn too. Grey colour level of filled points indicates the α_{TF} exponent used for each simulation: the palest grey for $\alpha_{TF}=3$, the darkest grey for $\alpha_{TF}=4$ and the intermediate grey level for $\alpha_{TF}=3.5$. *Inverse filled triangle*: Initial model. *Colored circles*: Mass ratio 1:2. *Colored squares*: Mass ratio 1:3. *Colored triangles*: Mass ratio 1:6. *Double centered symbol*: Retrograde models. *Crosses*: Observed bulges from APB95. *Asterisks*: Observed bulges from de Jong (1996b), re-analysed by G01. *Filled diamond point*: Initial model of ABP01. *Empty diamonds*: ABP01's remnants after the high-density satellite accretions.

3 Why does n increase

The evolution of the bulge profiles in the high-density experiments of ABP01 was driven by the puffing up of the bulge material and the deposition of the satellite's high density cusp in the remnant center. The dynamical mechanism for the increase of n in low-density models is different. In Figure 3 we show the time evolution of the primary disk and bulge particles to the surface brightness profile of the merger in model M3TF3D. The contribution of the satellite particles is plotted too. The satellite disrupts completely before reaching the galactic center, in such a way that this deposition over the remaining disk and the injection of disk material to the center are the responsible of the steepening of the profile.

Figure 4 shows the radii enclosing a given percentage of the mass for the particles initially belonging to the primary bulge for all the models. Our bulges basically expand their outer layers, while the 90% of their masses remains undisturbed. Then, bulge material puffing up can not be the responsible of the increasing of n in our low-density satellite accretions, contrary to what happened in ABP01's high-density experiments.

The distribution of material of each component in the final remnant of model M2TF4D is shown as a function of radius and height respect to the galactic plane in Figure 5. In the left panels, we have plotted the percentage respect to the total number of particles which initially belonged to each component at each galactic radius, r . Right panels represent the same as a function of the absolute value of the z -component. We have separated primary distributions (upper panels) from satellite contributions (lower panels) for clarity. Dashed lines indicate how the initial bulge and disk material were distributed, while solid lines correspond to the final acquired distribution by each of them in the upper panels. Dashed-dotted lines in the lower ones show final contributions of the satellite's bulge and disk material. Bulge and disk particles are differentiated by the grey scale (light and dark grey respectively) in both satellite and primary galaxy distributions. Looking at the upper panels, it is obvious that the distribution of particles associated to the primary bulge experiments little changes radially and vertically. Primary disk matter experiments an inward flow, as it can be noticed from Fig. 3. Their outer layers generate tails and expand due to tidal forces in the direct orbits, and are inhibited in the retrograde cases (Mihos & Hernquist, 1996). Satellite disk material rebuilds an exponential disk, following similar trends along the same range of R and $|z|$ than the primary disk material. However, satellite's bulge particles are confined to the remnant's inner region and to small values of $|z|$; i.e., satellite bulge material contributes to the thin disk. This effect is due to the fact that dynamical friction circularizes the orbit of the satellite prior to disruption: stars at the core of the satellite are more resilient to disruption and therefore end up on more circular orbits than those stripped earlier during the satellite decay process. As in Abadi et al. (2003a,b) simulations, most stars in the satellite are dispersed into a torus-like structure, whose radius is that at which final disruption takes place. This redistribution of material produces a population mixture which could be the responsible of the similar colors observed between bulges and disks (Peletier & Balcells, 1996).

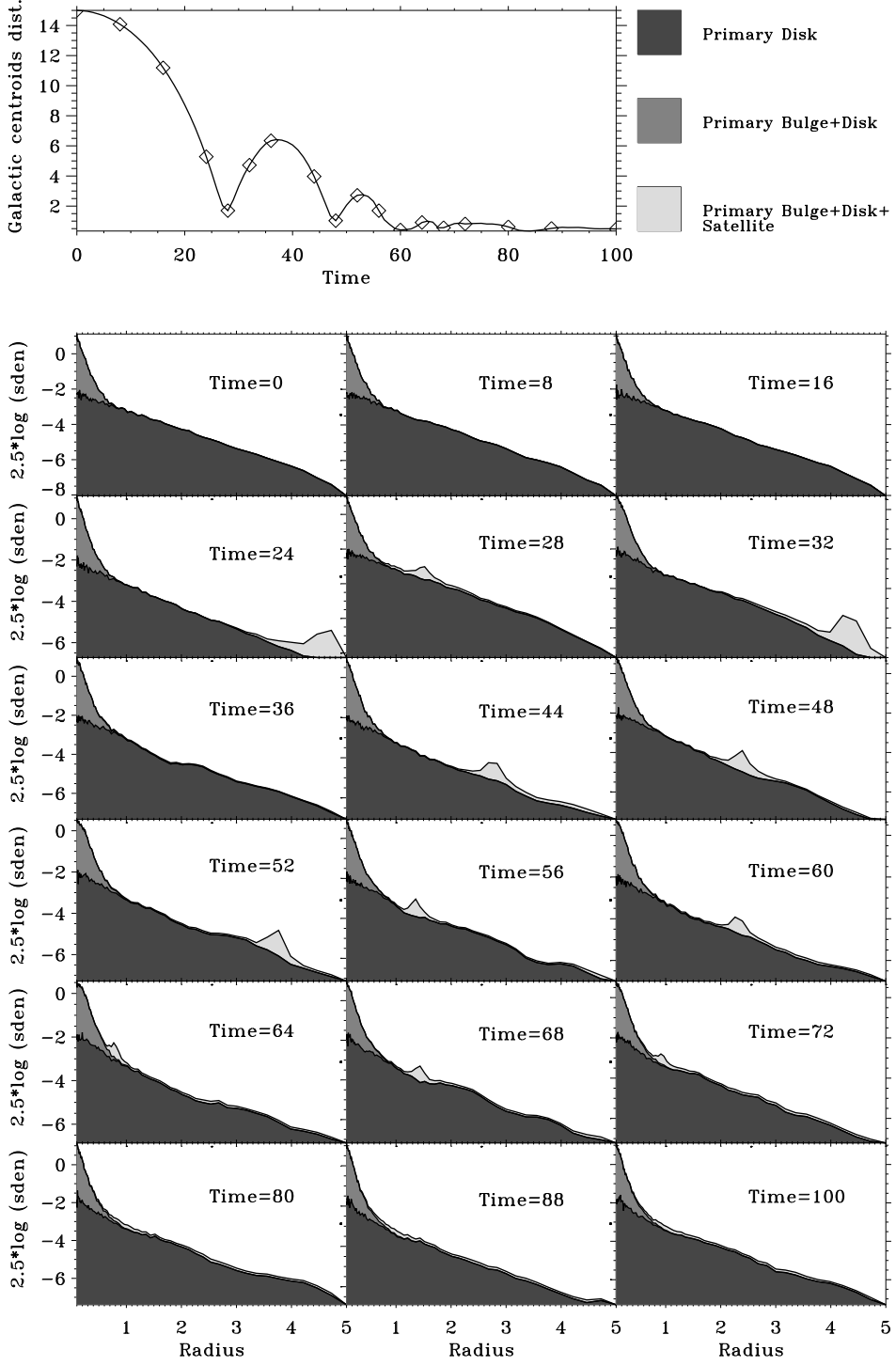


Figure 3: Evolution of the surface density profiles of the various luminous components. Contributions of each component to the total profile are drawn with different grey scales. Time is shown at upper right-corner of each frame. The first top panel shows the distance between centroids of the primary galaxy and the satellite as a function of time. *Darkest grey-filled region:* Contribution of the primary disk particles to the surface density profile at each time. *Intermediate grey-filled region:* Contribution of the primary bulge particles summed up to that of the disk primary material. *Palest grey-filled region:* Contribution of the satellite luminous material summed up to the luminous material of the primary galaxy.

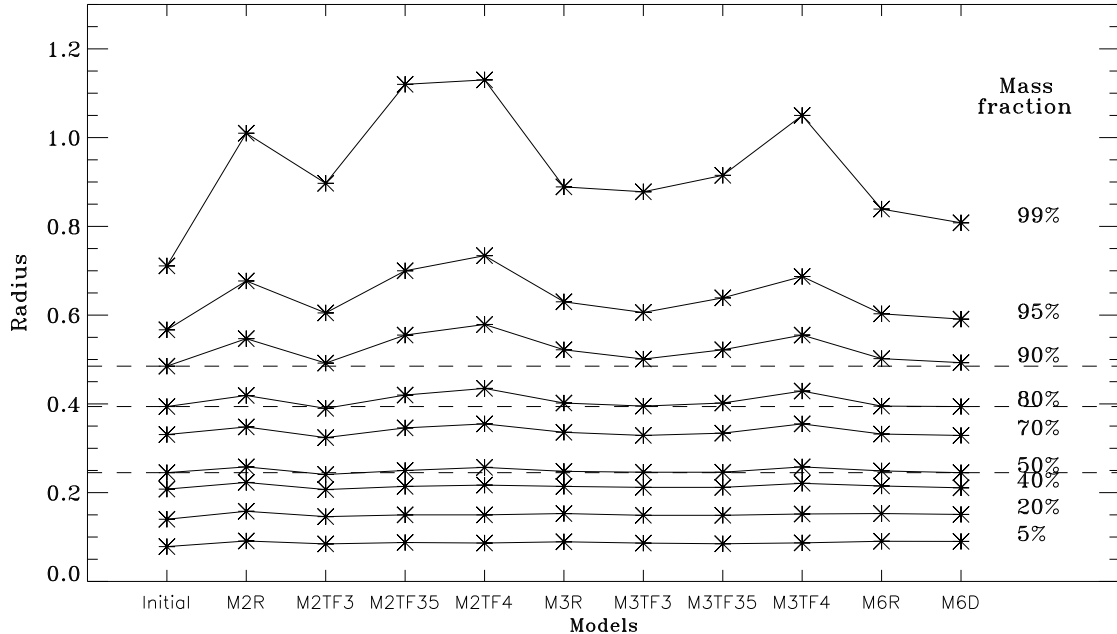


Figure 4: Radii enclosing a given % of the mass for the distribution of particles initially belonging to the bulge. The abscissa are the model codes from Table 2. The horizontal dotted lines are the radii initially enclosing a given % of the bulge mass, which appears next to the line, on the right of the Figure.

4 Scaling relations of disks and bulges

de Jong (1996a) and Courteau, de Jong, & Broeils (1996) observed that the ratio r_e/h_D between the bulge effective radius and the disk scale length is independent of Hubble type, and claimed that the spiral Hubble sequence is "scale-free". Balcells, Graham, & Peletier (2004b) (BGP04, hereinafter) confirm the independence of most disk-bulge structural parameters with Hubble type, but found that such photometric parameters of bulges and disks strongly correlate with bulge luminosity and with Sérsic index n . They conclude that galaxies themselves are not scale-free, the luminosity of the bulge being the critical scale.

In Figure 6, the dependences of the bulge and disk photometric parameters on the mass of the final bulge are shown, this last parameter obtained from the simultaneous Sérsic-exponential fits performed to the surface density profiles of the remnants. Supposing that the mass-to-light ratio M/L is constant and very similar for real bulges (Portinari, Somer-Larsen, & Tantalo, 2004), we have defined the bulge magnitude as $M_{Bul} \equiv -2.5 \cdot \log(Mass_{Bulge})$, because the bulge total mass can be directly related to its luminosity through the constant M/L . We have plotted ratios between the parameters of the final merger remnants and the corresponding to the initial galaxy vs. the increment in the bulge magnitude (i.e., final minus initial magnitude). Legend for symbols is the same as in Figure 2. Notice that the strong proportional relations be-

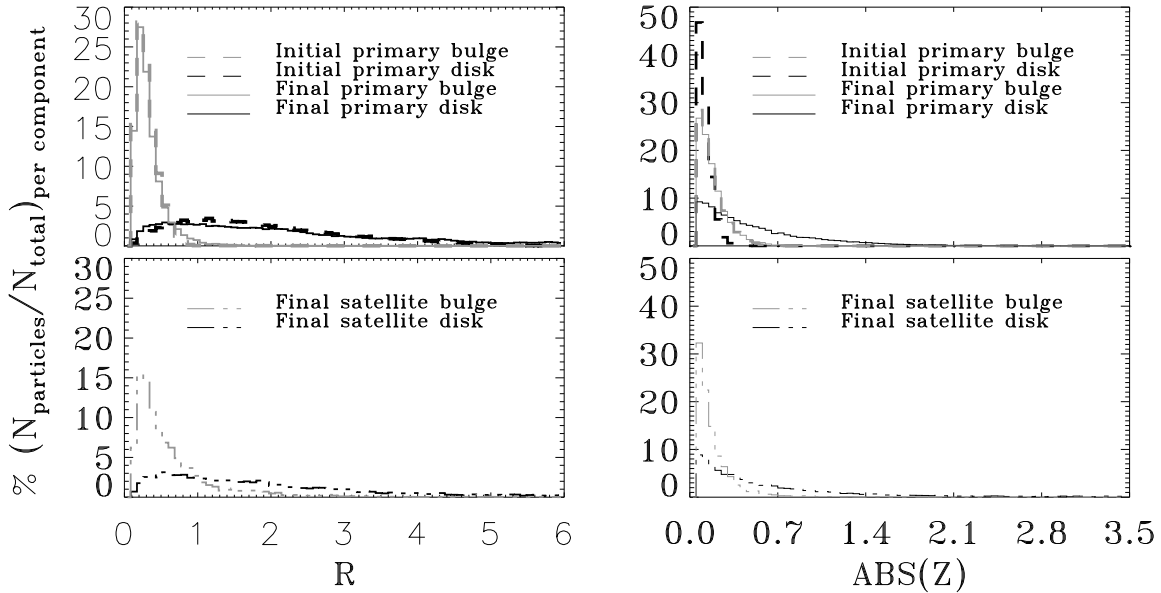


Figure 5: Distribution of material of each component in the final remnant of model M2TF4D. *Left panels*: Radial distribution of particles from each component in % respect to the total number which initially belonged to the same component. *Right panels*: The same as left panels, but vertically. *Dashed lines*: Initial distributions of disk and bulge particles from the primary galaxy. *Solid lines*: Final distributions of disk and bulge particles from the primary galaxy. *Dashed-dotted lines*: Final distributions of bulge and disk particles from the satellite in the remnant. Bulge and disk particles are colored by light and dark grey respectively in the three cases.

tween photometric parameters and the bulge magnitude in our low-density models are weaker in the ABP01's dense models (represented by empty diamonds in the Figure); trends as those exhibited by $\mu_{0,Bul}$, $n_{Sérsic}$, $\log(I_{0,Bul}/I_{0,Disk})$, $\log(B/D)$ and $\log(\sigma_0)$ (see panels (c), (f), (g), (i) and (k) in the Figure) correspond to correlation coefficients greater than 0.96 when a lineal fit is performed (you can see these values in Col. 6 from Table 4). This means that low-density satellite accretion processes do not alter galaxies randomly: they give place to remnants whose properties are scaled between them, depending on the mass ratios and the orbit of the encounter. In addition, all the remnants have brighter bulges than initially.

BGP04 gave mathematical expressions for the stronger relations, as follows:

$$\log(H) = (m \pm \Delta m) \cdot M_{K,Bulge} + (n \pm \Delta n) \quad (3)$$

where H represents a given photometric parameter (as $\mu_{0,Bulge}$, $\mu_{0,Disk}$, r_e , h_D , $n\dots$), or the ratio between two of them; $M_{K,Bulge}$ is the K-band bulge magnitude; and $(m \pm \Delta m)$ and $(n \pm \Delta n)$ are the slope and zero-point obtained from the orthogonal regression to the $\log(H)$ - $M_{K,Bulge}$ relation. We have performed linear fits to the relations shown at Figure 6, representing results by the dashed line in each case. Therefore, if real bulges grow through satellite accretions, our slopes should be similar to those found by BGP04, because our models are scalable and hence they can be displaced in the plane $\log(H)$ - $M_{K,bulge}$. The constants needed for transforming from masses to

luminosities and from a unit system to another do not affect the slopes in the relations, as they end as part of the additive term of the linear fit.

In Table 4, the slopes for all the strong correlations observed by BGP04 are compared to those obtained in our low-density models. It is encouraging that low-density models reproduce the observed tendencies in disk parameters, central velocity dispersions and B/D ratios. The correlations which we fail to reproduce with our experiments are those involving the bulge effective radius r_e (see r_e in panel (a) and r_e/h_D in panel (h) in the Figure). r_e becomes smaller with the accretion, while observed higher luminosity bulges have larger effective radii (Hubble, 1926; Binggeli, Sandage, & Tarenghi, 1984; Möllenhoff & Heidt, 2001, among others). This is due to the fact that the primary bulge material remains unaltered, while the bulge region receives a large inward piling up of disk particles that rises the central galactic brightness, making the effective radius decrease. On the other hand, the slope for the bulge central brightness $\mu_{0,Bulge}$ is very different from the observed value also, despite its sign is positive in both cases (see Table 4). Moreover, we find a correlation between the bulge effective brightness and $L_{K,bulge}$, while BGP04 do not detect a clear tendency in their sample of intermediate-to early-type spirals. Of course, these discrepancies remain important limitations of the current accretion models. Probably, these problems are associated to the fact that models without star formation and gas hydrodynamics implemented give an incomplete vision of the physical processes involved in the galactic accretions. These processes are known to affect central structure of real galaxies significantly (Mihos & Hernquist, 1996). Hence, all the relations found for the bulge parameters and ratios related to them must be distrusted. On the other hand, correlations involving large-scale parameters of the galaxy are well reproduced, probably because they are less affected by star formation.

5 Summary

The study of the effects of satellite infall onto galaxies needs to consider the dynamical transformations of the primary galaxy during the accretion (e. g. , triggering of spiral and bar distortions, redistribution of disk material), in addition to the deposition of accreted mass.

Low-density satellites that disrupt during their decay cause systematic structural transformations in the primary galaxy. It evolves towards higher B/D , higher n , higher σ_0 , higher h_D and lower $\mu_{0,Disk}$, all following trends similar to observations. A complete matching to present day galaxies may require the contribution of dissipative gas and star formation processes.

The infall of small, collapsed baryonic clumps is an inherent ingredient of galaxy formation models based on CDM (White & Rees, 1978). The models presented here might indicate that such infall drives pre-existing disks to a secular evolution toward

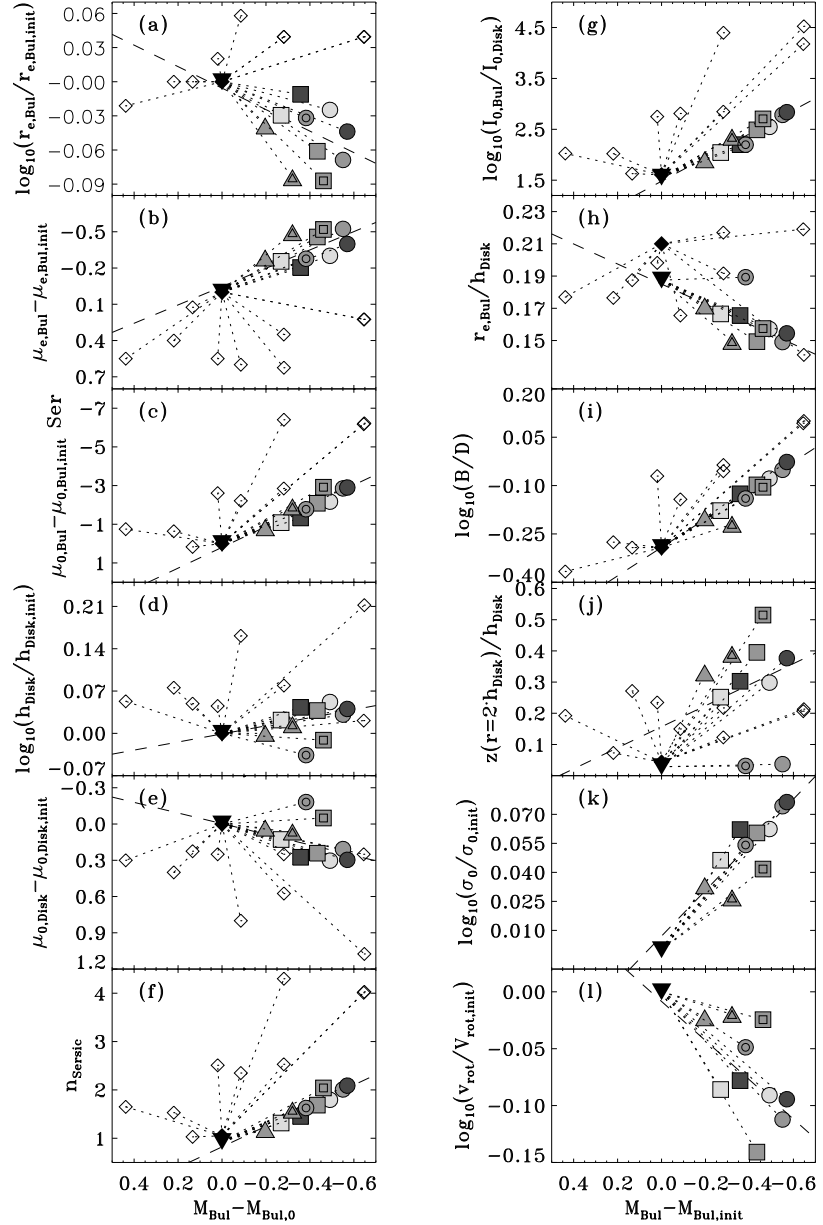


Figure 6: The dependence of bulge and disk parameters, and B/D ratios, on the bulge “magnitude”, defined as $M_{Bul} \equiv -2.5 \cdot \log(Mass_{Bul})$. All parameters are derived from Table 3. Legend is the same as in Figure 2. *Dashed lines*: Orthogonal regressions to the model points. Obtained slopes are compared to those from observations in Table 4. (a) Effective radius of the (Sérsic) bulge component. (b) Effective surface brightness of the Sérsic component. (c) Extrapolated central surface brightness of the Sérsic component. (d) Disk major-axis scale length. (e) Face-on extrapolated disk central surface brightness. (f) Sérsic index n . (g) Bulge-to-disk central brightness ratio $\log(I_{0,Bul}/I_{0,Disk})$. (h) Ratio r_e/h_D between the bulge effective radius and the major-axis disk scale length. (i) Bulge-to-disk luminosity ratio B/D . (j) Ratio $z_D(r=2 \cdot h_D)/h_D$ between the disk height scale at $r=2 \cdot h_D$ and the major-axis disk scale. (k) Central velocity dispersion. (l) Maximum rotational velocity.

Table 4: Photometric parameters slopes vs. bulge magnitude from our models and from BGP04 observations.

Photometric parameter (1)	Observational		Photometric parameter (4)	Modelled		
	Obs. Slope (2)	R_S (3)		Model Slope (5)	R_S (6)	χ^2 (7)
$\log(r_e/Kpc)$	-0.164 ± 0.028	-0.79	$\log(r_e/r_{e,inic})$	0.09 ± 0.04	0.41	0.004
$\mu_{e,K}/M_{K,\odot}$	no correlation	...	$\mu_e - \mu_{e,inic}$	0.76 ± 0.19	0.67	0.068
$\mu_{K,Ser}(0)/M_{K,\odot}$	0.92 ± 0.16	0.63	$\mu_{0,B} - \mu_{0,B,inic}$	5.4 ± 0.6	0.98	0.713
$\log(h_D/Kpc)$	-0.112 ± 0.016	-0.64	$\log(h_D/h_{D,inic})$	-0.07 ± 0.04	-0.73	0.003
$\mu_{K,D}(0)/M_{K,\odot}$	-0.30 ± 0.06	-0.63	$\mu_{0,D} - \mu_{0,D,inic}$	-0.44 ± 0.22	-0.80	0.094
$\log(I_{0,B}/I_{0,D})$	not significative	...	$\log(I_{0,B}/I_{0,D})$	-2.33 ± 0.17	-0.99	0.054
$\log(r_e/h_D)$	no correlation	...	$\log(r_e/h_D)$	0.062 ± 0.008	0.87	0.000
$\log(B/D)$	-0.30 ± 0.04	-0.80	$\log(B/D)$	-0.442 ± 0.018	-0.99	0.001
$n_{Sérsic}$	not significative	...	$n_{Sérsic}$	-2.13 ± 0.23	-0.99	0.107
...	z_D/h_D	-0.34 ± 0.09	-0.82	0.157
$\log(\sigma_0/km\ s^{-1})$	-0.13 ± 0.02	-0.81	$\log(\sigma_0/\sigma_{0,inic})$	-0.118 ± 0.019	-0.96	0.001
...	$\log(V_{rot}/V_{rot,inic})$	0.17 ± 0.07	0.67	0.009

Column description: Columns (1)-(3), fitted slopes of the correlations between photometric parameters and the K-band bulge magnitude, from the observational sample of intermediate- to early-type spirals by BGP04. Columns (4)-(7), fitted slopes for the equivalent correlations obtained from our models, using the corresponding structural parameters.

Columns: (1) Observational photometric parameter. (2) Observational fitted slopes of parameter in Col. 1 vs. $M_{K,Bul}$ from BGP04. (3) Observational correlation coefficient for the fit. (4) Structural parameters from our low-density models. (5) Fitted slopes of parameters in Col. 4 vs. $M_{Bul} - M_{Bul,0}$. (6) Correlation coefficient for the fit. (7) χ^2 of the fit.

higher B/D and n , through the inflow of primary disk material to the center via transitory bars, the deposition of satellite material rebuilding the exponential disk and the re-distribution of material vertically by heating. Secular evolution is currently being discussed as the outcome of bar instabilities in the disk due to gas cooling (Kormendy & Kennicutt, 2004). The present models could indicate that secular evolution can be due to satellite accretion as well. The latter might have been important at earlier galaxy ages.

References

Abadi, M.G., Navarro, J.F., Steinmetz, M., & Eke, V.R. 2003, ApJ, 591, 499A
 Abadi, M.G., Navarro, J.F., Steinmetz, M., & Eke, V.R. 2003, ApJ, 597, 21A
 Aguerri, J.A.L., Balcells, M., & Peletier, R.F. 2001, A&A, 367, 428 (ABP01)
 Andredakis, Y. C., Peletier, R. F., & Balcells, M. 1995, MNRAS, 275, 874
 Balcells, M., Graham, A.W., & Peletier, R.F. 2004, ApJ submitted, arXiv:astro-ph/0404379

Balcells, M., Graham, A.W., & Peletier, R.F. 2004, ApJ submitted, arXiv:astro-ph/0404381 (BGP04)

Binggeli, B., Sandage, A., & Tarenghi, M. 1984, AJ, 89, 64

Capaccioli, M., in IAU. Symp. 127, structure and Dynamics of Elliptical Galaxies, ed. P.T. de Zeeuw (Dordrecht: Reidel), 47

Courteau, S., de Jong., R. S., & Broeils, A. H. 1996, ApJ, 457, L73

de Jong, R. S. 1996, A&AS, 118, 557 (a)

de Jong, R. S. 1996, A&A, 313, 45 (b)

Eliche-Moral, M.C., Balcells, M., Aguerri, J.A.L., & González-García, A.C. 2005, in preparation

Graham, A.W. 2001, AJ, 121, 820 (G01)

Hernquist, L., & Katz, N. 1989, ApJS, 70, 419

Hubble, E.P. 1926, ApJ, 64, 321

Kormendy, J., & Kennicutt, R. C. Jr. 2004, ARA&A, 42, 603K

Kuijken, K., & Dubinski, J., 1995, MNRAS, 277, 1341

MacArthur, L.A., Courteau, S., & Holtzman, J.A. 2002, ApJ, 582, 689

Mihos, J.C., & Hernquist, L. 1996, ApJ, 464, 641

Möllenhoff, C., & Heidt, J. 2001, A&A, 368, 16

Peletier, R.F., & Balcells, M. 1996, AJ, 11, 2238

Portinari, L., Somer-Larsen, J., & Tantalo, R. 2004, MNRAS, 347, 691

Sérsic, J.L. 1968, Atlas de galaxias australes, Observatorio Astronómico, Córdoba

White, S.D.M., & Rees, M.J. 1978, MNRAS, 183, 341W